Investigation on Microstructure, Hardness and Wear Resistance of Electron Beam Wire-Feeding Deposited Inconel 718 Alloy Coatings

Dongheng Xu[1] · Han Wang[1] · Xuewei Tao[1] · Zhengjun Yao[1,2] · Shasha Zhang[1,2] · Moliar Oleksander[1,2]

Abstract

The Inconel 718 (IN718) alloy coatings were successfully fabricated using electron beam wire-feeding deposition technology. The macrostructure, microstructure and elemental analysis of the deposited coatings were characterized by OM, SEM and EDS. Moreover, the hardness and wear resistance were also investigated experimentally. The results showed that the cross section of the deposited coatings can be divided into three different regions: clad zone (CZ), fusion zone (FZ) and heat affected zone. Equiaxed dendrites appeared in the CZ while columnar dendrites occurred in the FZ, and discrete fine Laves phase particles were formed under low beam current while continuous coarse Laves phase particles were found under high beam current. The EDS results showed that the degree of Nb segregation in FZ is higher than that in CZ. More importantly, the microstructure coarsened and the degree of Nb segregation increased with the increase of beam current. The deposited coating under the lowest beam current (10 mA) has the highest hardness (263 HV0.2) and the minimum specific wear rate (3.95391×10^{-15} m^3/Nm), which is corresponding to the fine microstructure, discrete Laves phase particles and low degree of Nb segregation under low beam current.

Keywords Wire-feeding deposition · Electron beam · IN718 coating · Hardness · Wear resistance

1 Introduction

Additive manufacturing (AM) has been verified as a promising technique for component building and surface engineering, especially in aerospace and industrial applications, because of its very high efficiency in shortening time with respect to conventional processing approaches [1–3]. In terms of surface engineering, laser cladding technology has been widely investigated to obtain a repair or strengthening coating in the past years. Zhang et al. [4] repaired hemispherical defects on H13 tool steel substrates using laser direct deposition of Co-based alloy powders. They found that the repaired samples exhibit higher mechanical properties than the substrates. Li et al. [5] laser cladded a new type

Fe–Ni–Cr alloy coating on nodular cast iron, and the results showed that the cladding layers illustrated good combination of hardness, tensile property and wear resistance. Surface repairing and strengthening using laser cladding technology was also investigated in the literatures [6–9]. However, in the above mentioned laser cladding process, metal powders were used as the filler materials. There is a certain amount of powders cannot be caught by the melt pool during the powder deposition process [10]. The powders are blown to the surrounding environment, which causes potential hazard to the operators and the environment [11, 12]. Recent years, as one of the AM technology, electron beam wire-feeding deposition (EBWD) has attracted much attention for surface repairing and strengthening. EBWD is a rapid, cost-effective and flexible technology, which allows the use of premium wire materials with superior physical and chemical properties to obtain a metallurgical bonded coating to repair or strength the components which may have various defects caused by wear, oxidation and corrosion in service [13–15]. Compared to laser cladding, the wire-feeding deposition of EBWD has a higher deposition rate and material usage efficiency [16, 17]. Almost all the materials fed into the melt pool during the process are used to form the deposits, which

✉ Zhengjun Yao
 yaozj1921@126.com

1 College of Material Science and Technology, Nanjing University of Aeronautics and Astronautics, Nanjing 211106, China

2 Key Laboratory of Materials Preparation and Protection for Harsh Environment, Ministry of Industry and Information Technology, Nanjing 211106, China

| Table 1 Nominal chemical composition of the IN718 filler wire (wt%)	Ni	Cr	Fe	Nb	Mo	Ti	Al	Co	C	Mn	Si	P	S
	51.55	19.87	Remainder	4.92	3.56	1.09	0.63	< 1	< 0.08	< 0.35	< 0.35	< 0.015	< 0.015

lowers the risks to the operators and reduces the waste of materials. Besides, the metal wires are easily available and cheaper than powders, which makes the wire-feeding deposition very cost-competitive. Regarding heat source, the electron beam has higher energy density than laser, which offers it advantages such as minimal heat input, precise energy control to a localised region and a well-bonded clad layer [18]. Additionally, the EBWD process is conducted in a high vacuum environment in which the impurities in air can be effectively avoided. In view of these advantages of EBWD and its great potential in surface repairing and strengthening for aerospace and industrial components, such as turbine blades, landing gears and pressure containers [14, 17], it is necessary to investigate the suitability of this technology for surface engineering.

Inconel 718 (IN718) is a precipitation-hardenable Ni–Cr–Fe based superalloy widely used in highly aggressive working environments, which is an excellent repair and strengthen material because of its excellent mechanical properties, wear resistance, fatigue resistance, as well as outstanding welding performance [19, 20]. Most of researches have focused on the microstructures and mechanical properties of additive manufactured IN718 blocks [21–24]. However, few studies on the IN718 alloy coatings fabricated by EBWD technology have been reported. In this paper, IN718 alloy coatings were prepared on the surface of a carbon steel plate by using EBWD technology with different processing parameters, and the macrostructure, microstructure, hardness and wear resistance of the coatings were systemically investigated. This work would contribute insight on how the processing parameter of EBWD would influence the microstructure, hardness and wear resistance of the IN718 coatings, thus leading to high quality repairing or strengthening coatings with promising applications.

2 Experimental

The coatings were fabricated by a THL-8 kW model high power electron beam wire-feeding solid forming system. The substrate used for the deposition was a steel plate with a carbon content of 0.2%, and its dimension was 100 mm × 100 mm × 10 mm. The surface of the substrate was polished to remove the oxide film by abrasive paper and cleaned with acetone prior to the deposition. The IN718 wire, supplied by Special Metals Inc., with a diameter of 1.14 mm, was used as the deposition material and its nominal composition is listed in Table 1. The schematic of the
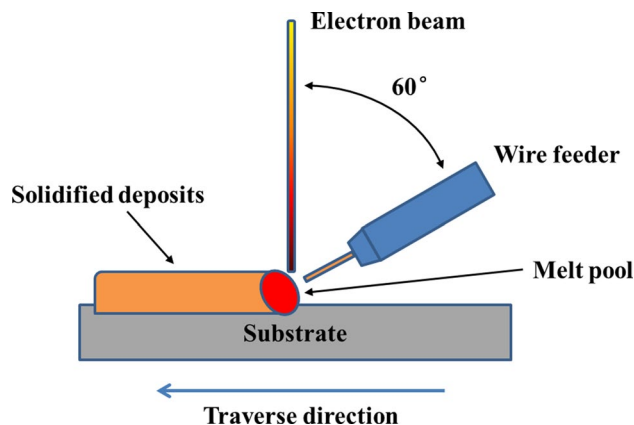
Fig. 1 Schematic of the EBWD process

Table 2 Processing parameters used in the experiments

Samples	U (kV)	I (mA)	V_t (mm/min)	V_w (mm/min)
A	60	10	300	324
B	60	12	300	324
C	60	14	300	324
D	60	16	300	324

EBWD process is presented in Fig. 1. The electron beam configuration was mounted on a CNC table having 3 degrees of freedom to traverse the substrate, and a vacuum system was employed to guarantee the forming chamber under a vacuum of 10^{-3} Pa to protect the molten metal during deposition process. The IN718 wire was axially fed into the melt pool generated by electron beam through a front feeding nozzle coupled with a synchronous wire feeder mechanism at an inclination angle of 30° from the surface of the substrate where interception with the incident electron beam occurred. In this work, single track coatings of different processing parameters were fabricated firstly to investigate the dimensions and macrostructures, and then multi-tracks coatings with an area of 40 mm × 40 mm were deposited with the selected processing parameters. The overlapping rate between two tracks is 50%, and each track was deposited along a single deposition direction. The processing parameters based on optimization experiments are selected as shown in Table 2, where the accelerate voltage "U" was fixed at 60 kV, the traverse speed of the substrate "V_t" and the wire feeding rate "V_w" were determined as 300 mm/min and 324 mm/min respectively, and the electron beam current "I" varied at four levels.

The deposited coupon was sectioned using a precision cut-off saw in a cross-section vertical to the traverse direction to extract specimens for microstructure observation and microhardness evaluation. After sectioning, the specimens were ground and polished to a surface finish of 0.04 μm, followed by chemical etching in aqua regia. Macrostructure and microstructure of the coatings were observed by an optical microscope (OM, SZN71) and a scanning electron microscope (SEM, ΣIGMA) equipped with an energy dispersive X-ray spectroscopy (EDS, Quantax). The microhardness of the deposited coatings was measured using a HX-1000TM Vickers microhardness tester with a load of 200 g and a dwell time of 15 s. Specimens with an area of 15 mm × 15 mm were cut from the deposited coupon for wear resistance testing using a sliding reciprocating tribotester (MFT-3000). The polished specimens were scratched against the GCr15 sphere with a diameter of 4.5 mm under dry sliding conditions, and the tests were performed at a constant normal load of 10 N with reciprocating frequency of 5 Hz and oscillating amplitude of 1 mm for 20 min. The cross-section profiles of each wear track at three positions were recorded via a profilometer (Alpha Step IQ). The volume loss was obtained based on the calculation of the cross-sectional area multiplied by the perimeter of the wear track. Then the wear rate was defined as the ratio of the wear volume loss over the normal load multiplied by the total slide distance [25]. Average of three replicas was reported as the final result. The morphology of wear tracks was observed by SEM, and the composition of wear debris was analyzed by EDS.

3 Results and Discussion

3.1 Macrostructure

Figure 2a–d shows the macro-morphology of the cross section of single track coatings under different beam current. For all of the samples, the cross section morphology can be clearly differentiated into three regions: clad zone (CZ), fusion zone (FZ) and heat affected zone (HAZ), and no obvious porosities and macro-cracks were found in the samples. Figure 2e demonstrates of the cross section of multi-tracks coating. It can be seen that several tracks overlapped to form a certain area, and the overlapping rate between two tracks is 50%. In order to further investigate the macrostructure of the deposited coatings, dimensional analyses were carried out with the single track samples. The dimensions of the single track samples under different beam current were measured according to the schematic in Fig. 3a. The macrostructure features of the single track samples can be estimated by aspect ratio (η) and dilution rate (ζ), and they are calculated according to following equations [26]:

$$\eta = w/h \tag{1}$$

$$\zeta = S_2/(S_1 + S_2) \tag{2}$$

where "w" is the width, "h" is the height, "S_1" is the area of CZ and "S_2" is the area of FZ, as schematically shown in Fig. 3a.

Figure 2a, b reveals sample A and B have the features of small aspect ratio and low dilution rate, while sample C and D have biggish aspect ratio and high dilution rate shown in Fig. 2c, d. The effect of beam current on the aspect ratio and dilution rate of the deposited coatings is indicated in Fig. 3b. It can be seen that both the aspect ratio and dilution ratio show an increasing tendency with the increase of beam current. There is a range of aspect ratio (about 2–7) which is favorable for processing efficiency and accuracy [27]. Thus the deposited coatings under low beam current (sample A and B) have the appropriate aspect ratio for improving the processing efficiency and accuracy, while the aspect ratio is too biggish to benefit the process under high beam current (sample C and D). Furthermore, a low dilution rate is an important criterion to evaluate a coating with high quality. Under low beam current, sample A and B have a low dilution rate which contributes to the substrate protection. For sample C and D under high beam current, the dilution rate is too high to remain the substrate material properties unchanged. Actually, there is a linear energy in the EBWD process, and it can be calculated as $E = U \cdot I/V_t$ [28]. The energy linearly depends on beam current when the traverse speed and wire feeding rate are determined. The heat input is low under small linear energy at low beam current, which results in low aspect ratio and dilution rate. In contrast, higher heat input under larger linear energy at higher beam current is corresponding with higher aspect ratio and dilution rate.

3.2 Microstructure

The SEM micrographs of CZ and FZ of the deposited coatings under different beam current are presented in Fig. 4. The micrographs of all samples show a typical dendritic microstructure which consists of non-uniform columnar dendrites and close-packed equiaxed dendrites. Nevertheless, the morphology of the dendrite demonstrates significant difference between the CZ and FZ of the coatings, and it also varies with the beam current. It can be obviously seen that the equiaxed dendrite appears in the CZ of all the coatings (Fig. 4a, c, e, g), while the columnar dendrite occurs in the FZ of all the coatings (Fig. 4b, d, f, h). This microstructure distinction between CZ and FZ is due to the ratio of the temperature gradient (G) to the growth rate (R) based on the solidification theory. Equiaxed growth of the dendrite appears at a low G/R ratio, while columnar growth occurs at a high G/R ratio [29]. At the initial stage of the solidification

Fig. 2 Cross section morphologies of the deposited coatings: single track coatings: sample A (**a**), sample B (**b**), sample C (**c**) and sample D (**d**); multi-tracks coating (**e**)
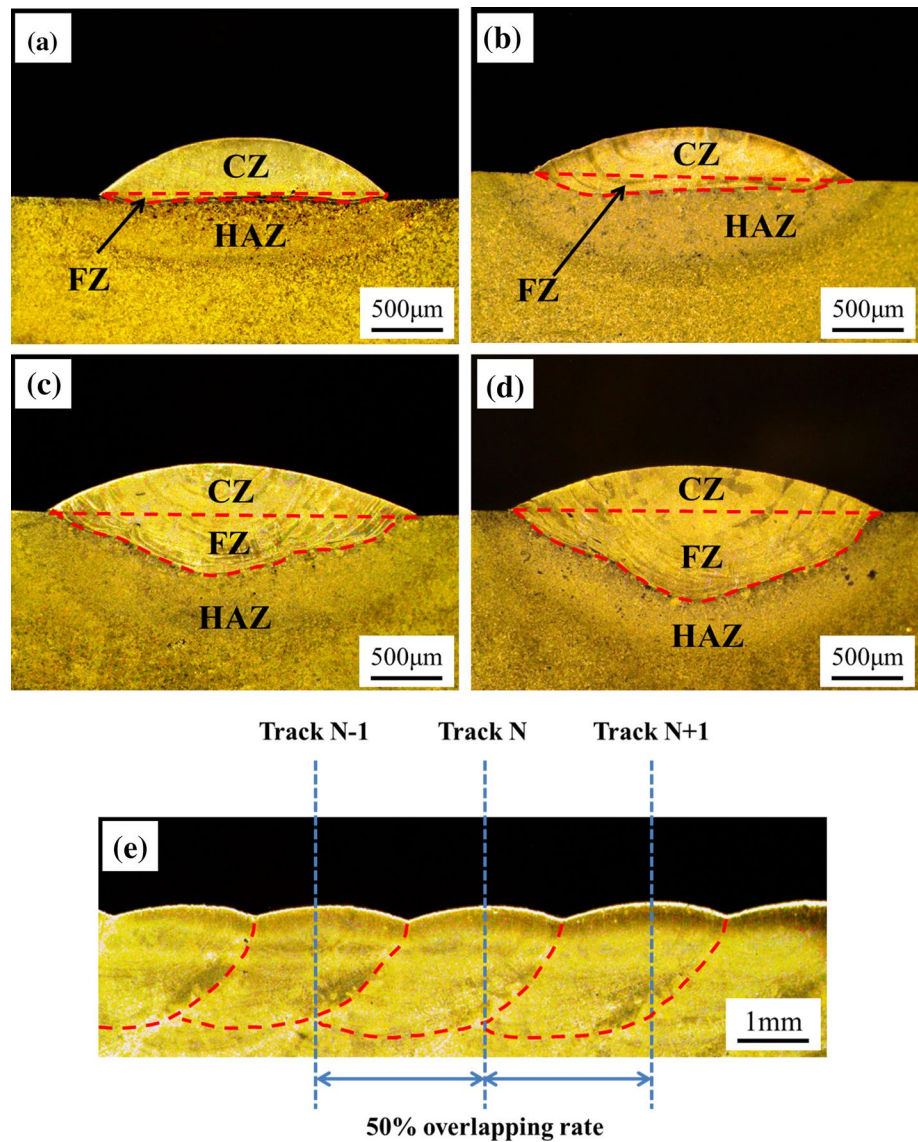
Fig. 3 Dimensional schematic (**a**) and the effect of beam current on dilution rate and aspect ratio (**b**) of single track coatings
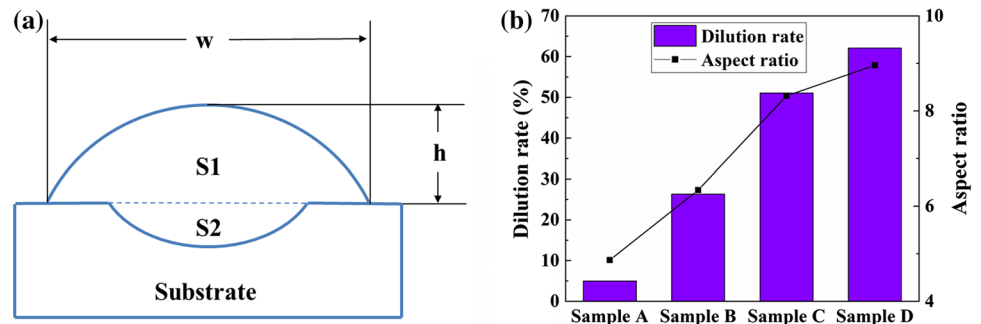

process, the substrate acts as a heat sink, the temperature gradient at the bottom of the molten pool is higher than that of other regions. Therefore, columnar dendrites form in the FZ of the coatings, and they grow almost along the direction of temperature gradient. In contrast, at the terminal stage of the solidification, the temperature gradient of CZ is lower than that of FZ since the heat dissipation of the melt pool is hindered by the bottom solidified structure with high temperature, which results in the formation of equiaxed dendrites in the CZ of the coatings. Remarkably,

Fig. 4 SEM micrographs of the deposited coatings: CZ (**a**) and FZ (**b**) of sample A; CZ (**c**) and FZ (**d**) of sample B; CZ (**e**) and FZ (**f**) of sample C; CZ (**g**) and FZ (**h**) of sample D
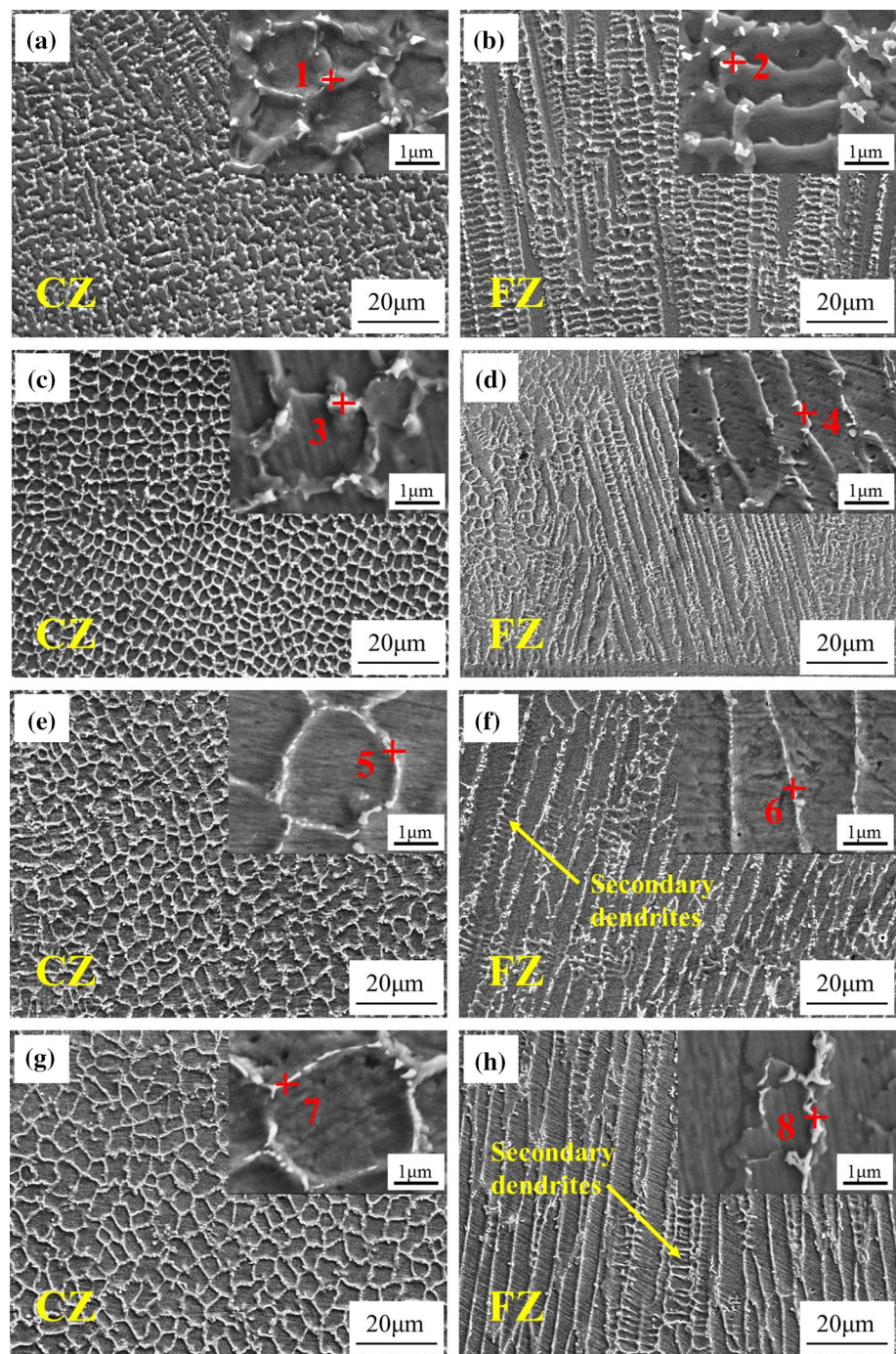
both the dendrites in CZ and FZ are varying with different beam current, as shown in Fig. 4. When the beam current is low, the columnar dendrites in FZ are lathy with a cellular structure (Fig. 4b, d). However, with the increasing of beam current, the columnar dendrites are becoming longer and coarser with some secondary dendrites (Fig. 4f, h). Meanwhile, the equiaxed dendrites in CZ under low beam current are fine, while the coarser equiaxed dendrites occur in CZ under high beam current, as shown in Fig. 4a, c, e, g. With the increase of beam current, the heat input of melt

pool increases, which consequently produces a larger and warmer melt pool. Thus the dendrites under high beam current have more thermal energy to grow coarser and longer than those under low beam current. Similar microstructures were observed in many laser deposited samples. Moussaoui et al. [30] investigated the microstructure of as-deposited IN718 fabricated by selective laser melting (SLM), which revealed that the morphology of dendrites is correlated to the volumetric energy density (VED) effect. Nie et al. [31] numerically simulated the microstructure evolution during

laser additive manufacturing of nickel-based superalloy and predicted similar microstructure. It is noteworthy that both the electron beam and laser deposition process are rapid solidification process, whereas the difference between them is diverse cooling rate [32].

As shown in Fig. 4, the microstructure of all samples consists of grey matrix and white precipitates, and the white precipitates are found in the inter-dendrite area. Previous works [33–35] have proved that the grey matrix is γ phase and the white precipitates are Laves phase. It can be clearly seen that the Laves phase in the CZ exhibits a circular pattern, and the circle becomes bigger with the increase of beam current. However, the Laves phase of chain pattern is found in the FZ and the chain becomes longer with the increase of beam current. From the inserted magnified graphs, discrete fine Laves phase particles are observed in sample A and B while the continuous coarse Laves phase particles are formed in sample C and D. The solidification condition has great effect on the morphology and size of Laves phase, such as the cooling rate and the ratio of temperature gradient to dendrite growth rate (G/R) [31, 36]. Under low beam current, sample A and B have low G/R ratio and high cooling rate during the solidification, giving rise to the formation of discrete fine Laves phase particles in the inter-dendritic area. For sample C and D with relatively high G/R ratio and low cooling rate under high beam current, it has continuous coarse Laves phase particles.

Nb is a critical element for the formation of Laves phase in IN718 alloy [37], which is attributed to the dependence of phase transition on the segregation of this element. In order to clarify the segregation of Nb in different region of the deposited coatings under different beam current, several spots shown in Fig. 4 were selected to analyze by EDS and the results are listed in Table 3. Interestingly, the concentration of Nb of the Laves phase in the CZ and FZ of the deposited coatings is discrepant, and it varies with the increase of beam current. According to Table 3, the concentration of Nb of spot 1, 3, 5, and 7 is lower than that of spot 2, 4, 6, and 8, respectively, which indicates that the Nb concentration of the Laves phase in CZ is lower than that in FZ. The different cooling rate between CZ and FZ may contribute to

the discrepant concentration of Nb of the Laves phase [38, 39]. With the increase of beam current, the mean concentration of Nb of the Laves phase for sample C and D is higher than that for sample A and B. For sample A and B with low beam current, the cooling rate is so fast, which indicates that more Nb atoms are dissolved in the γ austenite and a low degree of Nb segregation. Comparatively, for sample C and D with higher beam current, the cooling rate is relatively slow, which results in a higher degree of Nb segregation. In conclusion, all those results indicate that the segregation of Nb and the formation of Laves phase can be greatly suppressed under low beam current in the EBWD process.
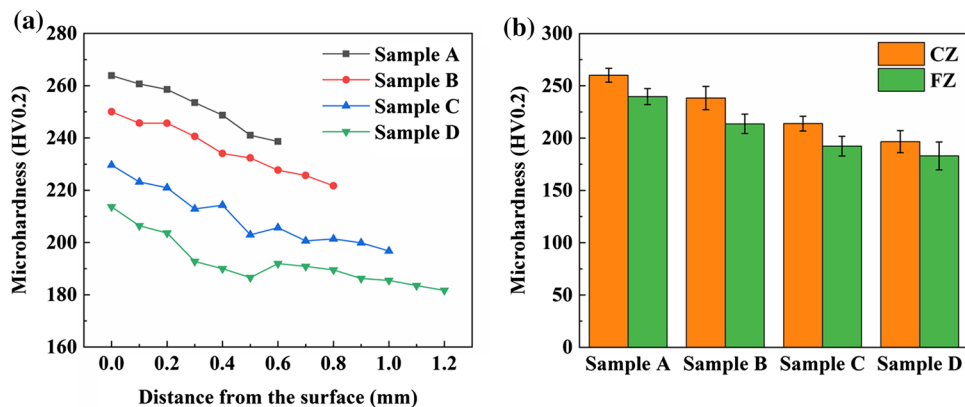
3.3 Hardness

Figure 5a shows the microhardness variations along the depth in the cross section of the deposited coatings under different beam current. Each value on the microhardness profile is the average of 5 test points in a horizon line perpendicular to the deposition direction. Interfaces between the CZ and FZ for individual profiles were located at 0.4–0.6 mm away from the surface of the coatings, depending on the macrostructure of the samples. It can be seen that the microhardness near the surface is the highest, and it is gradually decreases with the increase of the distance from the surface. The microhardness of sample A can reach about 263 HV0.2 near the surface which is the highest value among the samples. The hardness values of sample B, C and D decrease in turn, which indicates that the microhardness of the coating is reducing with the increasing of beam current. Literatures [40] and [41] investigated the Vickers hardness of IN718 coating fabricated by laser cladding technology, and the results showed that the hardness of the as-deposited coating is about 250 HV which is consistent with the hardness results of EBWD. They found that the variation of hardness was influenced by the Laves phase morphology and the refined Laves phase contributed to the increase of the hardness. As is illustrated in Fig. 4, the discrete fine Laves phase particles appear under low beam current while the continuous coarse Laves phase particles occur under high

Table 3 EDS results on the Laves phase in CZ and FZ of the deposited coatings

	Spectrum	Ni	Fe	Cr	Nb	Mo	Ti	Si
Sample A	1 (CZ)	49.56	18.84	12.77	11.08	4.09	2.34	1.33
	2 (FZ)	42.03	21.29	13.93	14.67	4.71	2.31	1.06
Sample B	3 (CZ)	35.16	32.92	11.46	12.14	4.24	2.56	1.52
	4 (FZ)	30.69	28.26	12.88	18.84	4.45	3.44	1.44
Sample C	5 (CZ)	23.5	38.23	8.16	18.81	4.92	4.62	1.75
	6 (FZ)	24.5	32.24	11.37	21.35	4.51	4.21	1.82
Sample D	7 (CZ)	15.58	49.23	6.1	19.90	4.24	3.87	1.07
	8 (FZ)	16.59	41.06	5.91	25.09	4.86	5.33	1.17

Fig. 5 Microhardness distribution of the deposited coatings: (**a**) microhardness variations along the depth; (**b**) average microhardness of the CZ and FZ

beam current. It may account for the decrease of the hardness as the increase of the beam current.

Figure 5b shows the average microhardness in the CZ and FZ of the deposited coatings under different beam current. For all of the samples, the average microhardness in the CZ is higher than that in the FZ. From the analysis in previous sections, the degree of Nb segregation in CZ is lower than that in FZ, which indicates that more Nb atoms are dissolved in the γ austenite in CZ. Therefore, the solid solution strengthening of Nb atoms facilitates the increase of microhardness in CZ [41], and the strengthening effect decreases with the increase of beam current. In addition, the difference of the microhardness between CZ and FZ is related to the different dendritic microstructures of them. The refined equiaxied dendrites in CZ contribute to the increase of the

microhardness. It is worthy to note that both the average microhardness of CZ and FZ of all the samples are higher than that of the substrate (175 HV0.2).

3.4 Wear Resistance

The typical friction coefficient curves, wear track profiles and specific wear rates of the deposited coatings are presented in Fig. 6. As shown in Fig. 6a, for all of the samples, the friction coefficient curves consist of two stages: decelerating wear stage and steady wear stage. The sample A shows a lower steady-stage friction coefficient with smaller fluctuation compared with other samples. With the increase of beam current, the friction coefficient increases and accompanied with a little bigger fluctuation. Figure 6b displays

Fig. 6 Typical friction coefficient (**a**), wear track profiles (**b**) and specific wear rates (**c**) of the deposited coatings
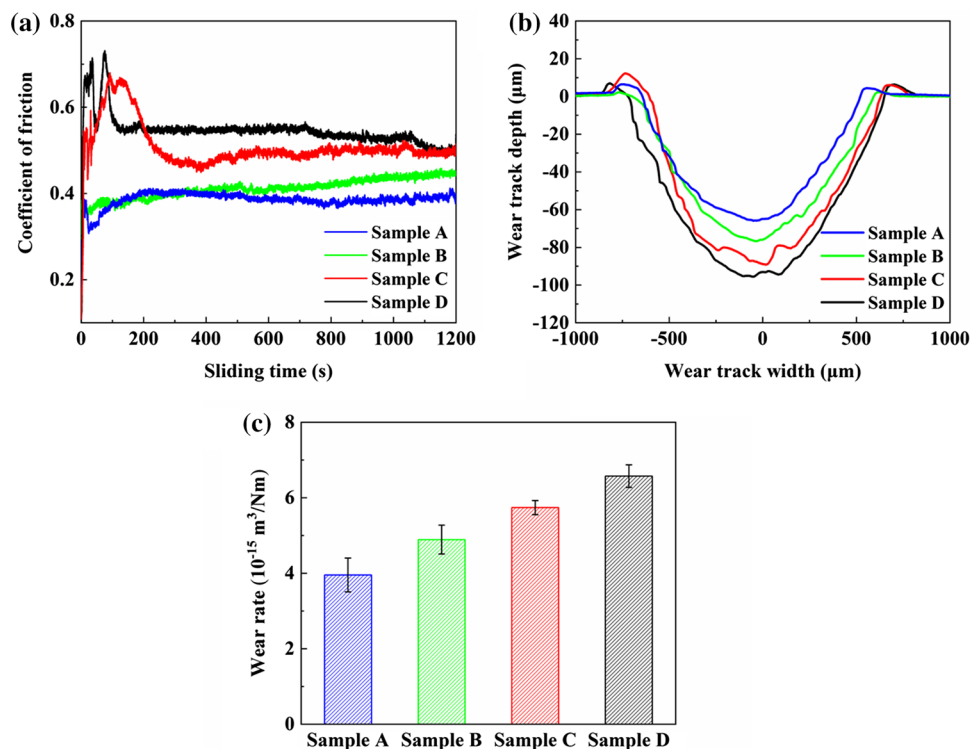
the typical wear track section profiles of the deposited coatings. It is obvious that the wear scar becomes wider and deeper with the increase of beam current. The specific wear rates of the deposited coatings are calculated and shown in Fig. 6c. As expected, the minimum specific wear rate (3.95391×10^{-15} m^3/Nm) was obtained for sample A, and the specific wear rate has an obvious increasing tendency with the increase of beam current.

The worn morphologies of the deposited coatings after wear resistance test were characterized by SEM and EDS, as shown in Fig. 7. It can be clearly seen from Fig. 7a, b that the sample A and B have some grooves parallel to the sliding direction, indicating the mechanism of the abrasive wear. The abrasive particles are found in the worn tracks of sample A and B, which may be is the Laves phase (EDS elemental analysis: Ni 43.28 at%, Fe 19.46 at%, Cr 13.98 at%, Nb 12.38 at%, Mo 3.99 at%, O 3.74 at%, Ti 2.05 at%, Si 1.12 at%). The existence of O element reveals the mechanism of oxidation wear, which is related to the elevated frictional heat and the high chemical activity of certain elements in IN718 alloy [42]. Besides, several small pits are also found in the worn tracks of sample A and B, which is the result of some small fragments were peeled off during the sliding process [43]. Comparatively, there are no evident grooves are observed in the wear tracks of sample C and D, but some obvious cracks and delamination appear in them, as shown in Fig. 7c, d. Due to the effect of plastic deformation in the friction process, the cyclic stress generated by sliding motion would be easily concentrated at the interfaces between precipitate phase and matrix [44, 45].

Thus the cracks generate and propagate near these weak regions and then the delamination emerges when the cracks further propagate to the ultimate, which is a typical feature of the fatigue wear [46, 47]. In the subsequent sliding process, the delamination transformed into spalling sheets and wear debris. For sample A and B under low beam current, the interface between discrete fine Laves phase and γ matrix is small, thus the crack is hard to propagate. However, the coarse Laves phase of sample C and D under high beam current provides a larger interface which contributes to the propagation of cracks. As a consequence, several pits formed in the worn tracks of sample A and B while large spalling sheets formed in the worn tracks of sample C and D. Curiously, the wear debris in the worn tracks of sample C and D has been severely oxidized (the white debris in Fig. 7c, d). The EDS analysis showed that the white debris is iron oxide (EDS elemental analysis: Fe 58.25 at%, O 32.97 at%, Cr 8.78 at%), indicating that the white wear debris is derived from the friction pair and it adhered to the worn surface. The adhesion is the result of "cold welding points" [48]. For samples under high beam current, the coarse microstructure and low hardness facilitate a severe plastic contact during the sliding process, which causes the cold welding occurs at the asperity contacts. In addition, the Fe element in friction pair and IN718 alloy is chemically active and has a high ductility, leading to a strong oxidation and adhesion tendency [49]. Therefore, the adhesive wear occurs and the wear debris has been oxidized in the subsequent sliding process. In summary, the wear mechanism for the deposited coatings under low beam current (sample A and B) is

Fig. 7 Worn morphologies of the deposited coatings: (**a**) sample A, (**b**) sample B, (**c**) sample C and (**d**) sample D
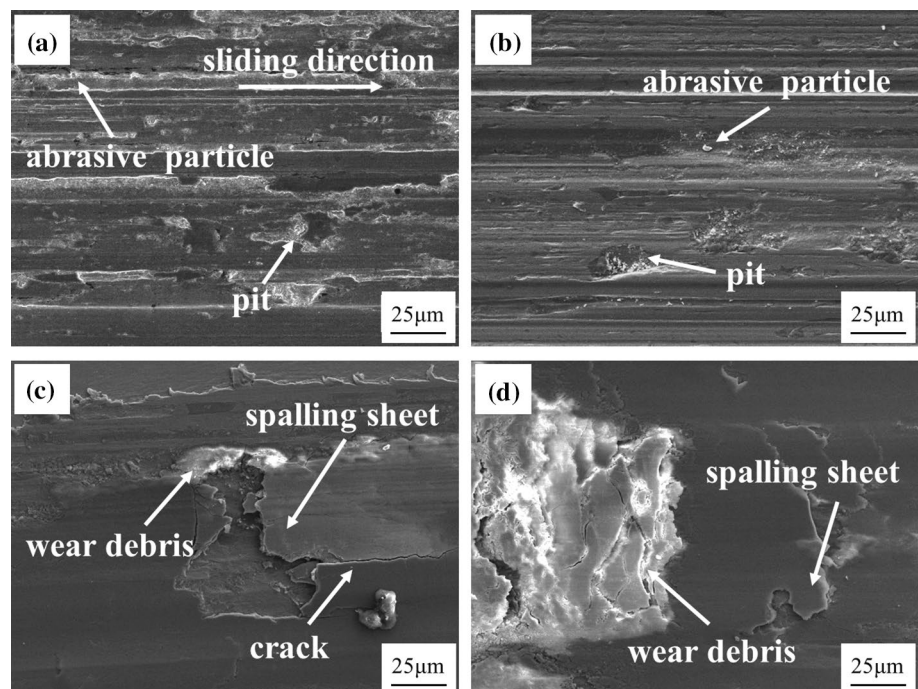
abrasive wear, fatigue wear and slight oxidation wear, while the fatigue wear, adhesive wear and severe oxidation wear are responsible for the deposited coatings under high beam current (sample C and D).

4 Conclusions

1. The IN718 alloy coatings were deposited by using EBWD technology with various beam currents. The cross section of the deposited coatings can be divided into three regions and the microstructures of these regions are discrepant.

2. Equaxied dendrites appear in the CZ while columnar dendrites occur in the FZ of the coatings, and the dendrites grow and coarsen with the increase of beam current. Discrete fine Laves phase particles are formed under low beam current while continuous chained Laves phase particles are found under high beam current.

3. The average Nb concentration of the Laves phase in CZ is lower than that in FZ, which is attributed to the higher cooling rate in the CZ. The degree of Nb segregation increases with the increase of beam current.

4. The average microhardness of CZ is higher than that of FZ, which is ascribed to the microstructure of CZ is finer than that of FZ. The wear resistance of the deposited coatings under low beam current is higher than that under high beam current. The wear mechanism of the deposited coatings under low beam current is abrasive wear, fatigue wear and slight oxidation wear, while the fatigue wear, adhesive wear and severe oxidation wear are responsible for the deposited coatings under high beam current.

Compliance with Ethical Standards

Conflict of interest The authors declare no conflict of interest.

References

1. M.A. Zaeem, A.J. Clarke, Rapid solidification and phase transformations in additive manufactured materials. JOM **68**(3), 928–929 (2016)
2. K. Eimann, M. Drach, K. Wissenbach, A. Gasser, *Proceedings of Stuttgarter Lasertage, Stuttgart, Germany* (2003)
3. A. Gasser, K. Wissenbach, R. Poprawe, Massgeschneiderte Oberflachen durch Laserstrahl-Oberflachenbehandlung mit Zusatzwerkstoffen-eine Ubersicht. Laser und Optoelektron **29**(3), 66–75 (1997)
4. X. Zhang, W. Li, X. Chen, W. Cui, F. Liou, Evaluation of component repair using direct metal deposition from scanned data. Int. J. Adv. Manuf. Technol. **95**(9–12), 3335–3348 (2018)
5. Y. Li, S. Dong, P. He, S. Yan, E. Li, X. Liu, B. Xu, Microstructure characteristics and mechanical properties of new-type FeNiCr laser cladding alloy coating on nodular cast iron. J. Mater. Process. Technol. **269**, 163–171 (2019)
6. J. Shi, S.Q. Bai, Research on gear repairing technology by laser cladding. Key Eng. Mater. **546**, 40–44 (2013)
7. D. Bartkowski, A. Młynarczak, A. Piasecki, B. Dudziak, M. Gościański, A. Bartkowska, Microstructure, microhardness and corrosion resistance of Stellite-6 coatings reinforced with WC particles using laser cladding. Opt. Laser Technol. **68**, 191–201 (2015)
8. D. Verdi, M.A. Garrido, C.J. Múnez, P. Poza, Mechanical properties of Inconel 625 laser cladded coatings: depth sensing indentation analysis. Mater. Sci. Eng. A **598**, 15–21 (2014)
9. Z. Zhang, P. Farahmand, R. Kovacevic, Laser cladding of 420 stainless steel with molybdenum on mild steel A36 by a high power direct diode laser. Mater. Des. **109**, 686–699 (2016)
10. S.H. Mok, G. Bi, J. Folkes, I. Pashby, Deposition of Ti–6Al–4V using a high power diode laser and wire, part I: investigation on the process characteristics. Surf. Coat. Technol. **202**(16), 3933–3939 (2008)
11. I.R. Pashby, S.H. Mok, J. Folkes, *23rd International Congress on Applications of Lasers and Electro-optics, San Francisco, USA* (2004), p. 18
12. C. Ader, M. Brosemer, C. Freyer, H. Fricke, D. Hennings, F. Klocke, V. Kühne, W. Meiners, C. Over, H. Pleteit, S. Stührmann, I. Wirth, T. Wirtz, K. Wissenbach, *Solid Freeform Fabrication Symposium, Austin, TX, USA* (2004), p. 26
13. H.B. Suo, Z.Y. Chen, J.R. Liu, S.L. Gong, J.Z. Xiao, Microstructure and mechanical properties of Ti–6Al–4V by electron beam rapid manufacturing. Rare Met. Mater. Eng. **43**(4), 780–785 (2014)
14. J. Gocke, J. Beuth, K. Taminger, Integrated control of solidification microstructure and melt pool dimensions in electron beam wire feed additive manufacturing of Ti–6Al–4V. Addit. Manuf. **1**, 119–126 (2014)
15. R.W. Bush, C.A. Brice, Elevated temperature characterization of electron beam freeform fabricated Ti–6Al–4V and dispersion strengthened Ti–8Al–1Er. Mater. Sci. Eng. A **554**, 12–21 (2012)
16. K. Taminger, R.A. Hafley, Electron beam freeform fabrication: a rapid metal deposition process, in *Proceedings of the 3rd Annual Automotive Composites Conference* (Society of Plastics Engineers, Troy, 2003)
17. K.M. Taminger, R.A. Hafley, *Electron Beam Freeform Fabrication (EBF3) for Cost Effective Near-Net Shape Manufacturing*. NASA Technical Memorandum TM-2006-214284
18. C. Körner, Additive manufacturing of metallic components by selective electron beam melting—a review. Int. Mater. Rev. **61**(5), 361–377 (2016)
19. M. Anderson, R. Patwa, Y.C. Shin, Laser-assisted machining of Inconel 718 with an economic analysis. Int. J. Mach. Tool Manuf. **46**(14), 1879–1891 (2006)
20. K.H. Song, K. Nakata, Microstructural and mechanical properties of friction-stir-welded and post-heat-treated Inconel 718 alloy. J. Alloys Compd. **505**(1), 144–150 (2010)
21. Q. Jia, D. Gu, Selective laser melting additive manufactured Inconel 718 superalloy parts: high-temperature oxidation property and its mechanisms. Opt. Laser Technol. **62**, 161–171 (2014)
22. M.M. Kirka, K.A. Unocic, N. Raghavan, F. Medina, R.R. Dehoff, S.S. Babu, Microstructure development in electron beam-melted Inconel 718 and associated tensile properties. JOM **68**(3), 1012–1020 (2016)

23. S. Sui, H. Tan, J. Chen, C. Zhong, Z. Li, W. Fan, A. Gasser, W. Huang, The influence of Laves phases on the room temperature tensile properties of Inconel 718 fabricated by powder feeding laser additive manufacturing. Acta Mater. **164**, 413–427 (2018)

24. R.K. Bird, J. Hibberd, *Tensile Properties and Microstructure of Inconel 718 Fabricated with Electron Beam Freeform Fabrication (EBF3)*. NASA Technical Memorandum TM-2009-215929

25. Z. Qiu, P. Zhang, D. Wei, B. Duan, P. Zhou, Tribological behavior of CrCoNiAlTiY coating synthesized by double-glow plasma surface alloying technique. Tribol. Int. **92**, 512–518 (2015)

26. Y. Zhang, J. Huang, P. Nie, H. Liu, Z. Li, Y. Wu, An investigation on high power diode laser cladding of Ni–Fe–Cr based alloy coatings. Rare Met. Mater. Eng. **41**, 199–202 (2012)

27. P.K. Farayibi, T.E. Abioye, A.T. Clare, A parametric study on laser cladding of Ti–6Al–4V wire and WC/W2C powder. Int. J. Adv. Manuf. Technol. **87**(9–12), 3349–3358 (2016)

28. A. Mohammad, A. Alahmari, M. Mohammed, R. Renganaya-galu, K. Moiduddin, Effect of energy input on microstructure and mechanical properties of titanium aluminide alloy fabricated by the additive manufacturing process of electron beam melting. Materials **10**(2), 211 (2017)

29. Z.G. Gao, O.A. Ojo, Modeling analysis of hybrid laser-arc welding of single-crystal nickel-base superalloys. Acta Mater. **60**(6–7), 3153–3167 (2012)

30. K. Moussaoui, W. Rubio, M. Mousseigne, T. Sultan, F. Rezai, Effects of selective laser melting additive manufacturing parameters of Inconel 718 on porosity, microstructure and mechanical properties. Mater. Sci. Eng. A **735**, 182–190 (2018)

31. P. Nie, O.A. Ojo, Z. Li, Numerical modeling of microstructure evolution during laser additive manufacturing of a nickel-based superalloy. Acta Mater. **77**, 85–95 (2014)

32. C.W. White, M.J. Aziz, Energy deposition, heat flow, and rapid solidification during laser and electron beam irradiation of materials, in *Surface Alloying by Ion, Electron, and Laser Beams* (American Society for Metals, Metals Park, 1986), pp. 19–50

33. H. Qi, M. Azer, A. Ritter, Studies of standard heat treatment effects on microstructure and mechanical properties of laser net shape manufactured INCONEL 718. Metall. Mater. Trans. A **40**(10), 2410–2422 (2009)

34. Y.C. Zhang, Z.G. Li, P.L. Nie, Y.X. Wu, Effect of heat treatment on niobium segregation of laser-cladded IN718 alloy coating. Metall. Mater. Trans. A **44**(2), 708–716 (2013)

35. K.D. Ramkumar, R.J. Sai, V.S. Reddy, S. Gundla, T.H. Mohan, V. Saxena, N. Arivazhagan, Effect of filler wires and direct ageing on the microstructure and mechanical properties in the multi-pass welding of Inconel 718. J. Manuf. Process. **18**, 23–45 (2015)

36. J. Lambarri, J. Leunda, V.G. Navas, C. Soriano, C. Sanz, Microstructural and tensile characterization of Inconel 718 laser coatings for aeronautic components. Opt. Lasers Eng. **51**(7), 813–821 (2013)

37. Y.T. Long, P.L. Nie, Z.G. Li, J. Huang, L.I. Xiang, X.M. Xu, Segregation of niobium in laser cladding Inconel 718 superalloy. Trans. Nonferr. Met. Soc. China **26**(2), 431–436 (2016)

38. T. Antonsson, H. Fredriksson, The effect of cooling rate on the solidification of Inconel 718. Metall. Mater. Trans. B **36**(1), 85–96 (2005)

39. S.G.K. Manikandan, D. Sivakumar, K.P. Rao, M. Kamaraj, Effect of weld cooling rate on Laves phase formation in Inconel 718 fusion zone. J. Mater. Process. Technol. **214**(2), 358–364 (2014)

40. H. Xiao, S.M. Li, W.J. Xiao, Y.Q. Li, L.M. Cha, J. Mazumder, L.J. Song, Effects of laser modes on Nb segregation and Laves phase formation during laser additive manufacturing of nickel-based superalloy. Mater. Lett. **188**, 260–262 (2016)

41. Y. Zhang, L. Yang, J. Dai, J. Liu, W. Zhang, H. Chen, Z. Wang, K. Shi, Microstructure and mechanical properties of pulsed laser cladded IN718 alloy coating. Surf. Eng. **34**(4), 259–266 (2018)

42. C. Cai, B. Song, C.L. Qiu, L.F. Li, P.J. Xue, Q.S. Wei, J.X. Zhou, H. Nan, H.X. Chen, Y.S. Shi, Hot isostatic pressing of in situ TiB/Ti–6Al–4V composites with novel reinforcement architecture, enhanced hardness and elevated tribological properties. J. Alloys Compd. **710**, 364–374 (2017)

43. J.B. Cheng, X.B. Liang, Z.H. Wang, B.S. Xu, Dry sliding friction and wear properties of metallic glass coating and martensite stainless coating. Tribol. Int. **60**, 140–146 (2013)

44. H. Yang, Y. Liu, T. Zhang, H. Wang, B. Tang, J. Qiao, Dry sliding tribological properties of a dendrite-reinforced Zr-based bulk metallic glass matrix composite. J. Mater. Sci. Technol. **30**(6), 576–583 (2014)

45. P.K. Farayibi, *Laser Cladding of Ti–6Al–4V with Carbide and Boride Reinforcements Using Wire and Powder Feedstock*, PhD thesis (University of Nottingham, Nottingham, 2014)

46. L.L. Guo, L. Qin, F.Y. Kong, H. Yi, B. Tang, Improving tribological properties of Ti–5Zr–3Sn–5Mo–15Nb alloy by double glow plasma surface alloying. Appl. Surf. Sci. **388**, 203–211 (2016)

47. X.W. Tao, Z.J. Yao, X.X. Luo, Comparison of tribological and corrosion behaviors of Cp Ti coated with the TiO_2/graphite coating and nitrided TiO_2/graphite coating. J. Alloys Compd. **718**, 126–133 (2017)

48. S. Bruschi, R. Bertolini, A. Ghiotti, Coupling machining and heat treatment to enhance the wear behaviour of an additive manufactured Ti6Al4V titanium alloy. Tribol. Int. **116**, 58–68 (2017)

49. F.H. Stott, J. Glascott, G.C. Wood, The sliding wear of commercial Fe–12% Cr alloys at high temperature. Wear **101**(4), 311–324 (1985)